Nano Research 2016, 9(12): 3881–3892
DOI 10.1007/s12274-016-1257-9
Research Article
ISSN 1998-0124
CN 11-5974/O4

A highly durable catalyst based on $Co_xMn_{3-x}O_4$ nanosheets for low-temperature formaldehyde oxidation

Yongchao Huang[1,§], Kaihang Ye[2,§], Haibo Li[1], Wenjie Fan[1], Fengyi Zhao[1], Yuanming Zhang[2] (✉), and Hongbing Ji[1] (✉)

[1] *MOE of the Key Laboratory of Bioinorganic and Synthetic Chemistry, KLGHEI of Environment and Energy Chemistry, The Key Lab of Low-carbon Chemistry and Energy Conservation of Guangdong Province, School of Chemistry and Chemical Engineering, Sun Yat-Sen University, Guangzhou 510275, China*

[2] *Country Department of Chemistry, Jinan University, Guangzhou 510632, China*

[§] *These authors contributed equally to this work.*

Received: 14 June 2016
Revised: 27 July 2016
Accepted: 21 August 2016

KEYWORDS

$Co_xMn_{3-x}O_4$ nanosheet, formaldehyde, catalytic oxidation, mechanism

ABSTRACT

Cost-effective catalysts for the oxidation of volatile organic compounds (VOCs) are critical to energy conversion applications and environmental protection. The main bottleneck of this process is the development of an efficient, stable, and cost-effective catalyst that can oxidize HCHO at low temperature. Here, an advanced material consisting of manganese cobalt oxide nanosheet arrays uniformly covered on a carbon textile is successfully fabricated by a simple anodic electrodeposition method combined with post annealing treatment, and can be directly applied as a high-performance catalytic material for HCHO elimination. Benefiting from the increased surface oxygen species and improved redox properties, the as-prepared manganese cobalt oxide nanosheets showed substantially higher catalytic activity for HCHO oxidation. The catalyst completely converted HCHO to CO_2 at temperatures as low as 100 °C, and exhibited excellent catalytic stability. Such impressive results are rarely achieved by non-precious metal-based catalysts at such low temperatures.

1 Introduction

With ever-increasing concerns on indoor formaldehyde (HCHO) pollution caused by urea-formaldehyde insulation finishing materials and the degassing of particle board and sealants, there have been much efforts to seek an effective method for its removal [1–6]. In recent years, thermal catalytic oxidation of indoor HCHO to CO_2 has been considered one of the most promising environmental technologies [7–10]. The key issue for the thermal catalytic oxidation is the availability of an effective catalyst [11–13]. In the past few years, supported precious metal catalysts (e.g., Pt, Pd and Au) have been studied for the catalytic oxidative removal of indoor HCHO [3, 14, 15]. Although

Address correspondence to Yuanming Zhang, tzhangym@jnu.edu.cn; Hongbing Ji, jihb@mail.sysu.edu.cn

the supported Pt and Pd catalysts have shown good catalytic activity at low temperatures, their wide application is hindered by their high cost, low thermal stability, easy sintering, and tendency to be poisoned [16–18]. To this end, it is vital to develop alternative cost-effective catalysts with high efficiency for the oxidation of indoor HCHO at low temperatures.

Transition metal oxides such as Co_3O_4 have been extensively researched as a promising effective alternative for HCHO catalytic oxidation [19, 20]. However, due to the fact that cobalt is toxic and expensive, and importantly due to its low redox reactivity, serious efforts are being made towards replacing Co_3O_4 partially with eco-friendly and cheaper metals [21]. Recently, spinel manganese cobaltite, obtained by partially replacing cobalt atoms with manganese, has been conceived as a promising cost-effective and scalable alternative for HCHO oxidation owing to its several inherent advantages including low cost, abundance, and good environmental benignity [22, 23]. Additionally, this binary metal oxide (BMO), possesses a much higher activity than manganese oxides or cobalt oxides because of the coupling of two metal species, rendering the BMO richer redox reactivity than the individual metal oxides. These properties are beneficial for catalytic oxidation applications [23, 24]. Further, the various combinations of cations and the tunable stoichiometric/non-stoichiometric compositions of the BMOs provide vast opportunities for manipulation of their physical and chemical properties [2].

As far as field applications are concerned, the usage of metal oxides in their powder form, especially as nanoparticles, has several limitations such as difficulties in the process, possibility of dust contamination, and the leaching of nanoparticles along with the treated exhaust gas [25, 26]. The direct synthesis of catalysts with excellent mechanical properties on a solid support is highly desirable for catalytic applications. Flexible carbon textiles have a porous structure and are composed of fibers that are three-dimensionally connected with each other. They are abundantly available, economical, renewable, have unique mechanical and thermal properties, are environment friendly, and are increasingly gaining interest as a flexible support for catalysts [27]. The macropore structure of carbon fibers helps in significant reduction of air resistance in gas phase reactions. In this study, we develop a facile method to fabricate arrays of Co-Mn precursor-based hierarchical structures on a carbon textile substrate. These structures are then converted into their porous $Co_xMn_{3-x}O_4$ counterparts via post-annealing. Moreover, the molar ratio of Mn to Co can be tuned within the final product. Significantly, the obtained $Co_xMn_{3-x}O_4$ (x = 0.65) nanosheets exhibit superior catalytic activity and stability. It can convert 100% of HCHO at a low temperature of 100 ℃ and has excellent catalytic stability for 300 h with less than 3% decrease in HCHO conversion efficiency.

2 Experimental

2.1 Preparation of $Co_xMn_{3-x}O_4$ nanosheets

Co-Mn oxides with different Mn/Co atomic ratios were prepared by anodic electrodeposition onto a carbon textile substrate. Electrodeposition was conducted in a solution (15 mL) containing manganese nitrate (0.02 M), cobalt chloride (0.02 M), and dimethyl sulfoxide (10 % v/v) at 70 ℃ with a current of 0.2 mA for 60 min. The Co-Mn precursor nanosheets were annealed in air at 550 ℃ for 1 h. The molar ratio between $Mn(NO_3)_2$ and $CoCl_3$ was controlled at 1:1, 1:2, 1:4, 2:1 and 4:1. MnO_x and CoO_x nanowires were deposited on the carbon textile under the same conditions for comparison.

2.2 Material characterization

Field-emission scanning electron microscopy (SEM, JSM-6330F) and transmission electron microscopy (TEM, JEM2010-HR) were carried out to characterize the morphology of the $Co_xMn_{3-x}O_4$ catalysts. X-ray photoelectron spectroscopy (XPS, ESCALab250) and X-ray diffraction (XRD, D8 ADVANCE, Bruker) with Cu Kα radiation (λ = 1.5418 Å) were performed to characterize the crystal phases of $Co_xMn_{3-x}O_4$ catalysts. T-5080 Autochem analyzer with a thermal conductivity detector was used to analyze the temperature-programmed reduction (TPR) of $Co_xMn_{3-x}O_4$ catalysts. The catalysts (50 mg) were loaded in a tube-shaped cell with an atmosphere of 10% H_2 in N_2 at a flow rate of 50 mL·min^{-1}. The TPR profiles were recorded between 35 and 800 ℃ at a heating rate of 10 ℃·min^{-1}.

The O_2-temperature- programmed desorption (TPD) is also carried out by the T-5080 Autochem analyzer, where the catalysts are first treated at 300 ˚C under a He atmosphere with 5% of O_2 (50 mL·min^{-1}). After the temperature decreased below 40 ˚C, the catalysts adsorbed enough O_2 and then the carrier gas was changed to pure He. The temperature was programmed to increase to 450 ˚C (10 ˚C·min^{-1}). The nitrogen adsorption and desorption isotherms were recorded at 77 K by an Autosorb-1 apparatus and the specific surface areas are calculated according to a multipoint Brunauer–Emmett–Teller analysis. *In situ* diffuse reflectance infrared Fourier transform spectroscopy (DRIFTS) was measured on an EQVINOX-55 FFT spectroscope apparatus (Bruker). The catalysts (10 mg) were placed in a ceramic crucible in a gas chamber. Formaldehyde was bubbled into the chamber with N_2 and the total gas flow rate was maintained at 100 mL·min^{-1}. The spectra were recorded as an average of 64 scans with a resolution of 4 cm^{-1} under reaction conditions. The CO_2 in the gas phase was determined with an online mass spectrometer (MS, Pfeiffer Omni-star GSD-301).

2.3 Measurement of catalytic activity

HCHO oxidation was carried out in a fixed-bed reactor with catalyst (0.85 g). HCHO gas was produced by injecting purified air (N_2/O_2 = 4,100 mL·min^{-1}) into an incubator, which was filled with a solution of 37% HCHO and maintained at 0 ˚C. The gas hourly space velocity (GHSV) under these conditions is 120,000 mL·h^{-1}·g^{-1}. The phenol spectrophotometric method was performed to detect the HCHO concentration. In this method, the gas was injected into 5 mL of $C_6H_4SN(CH_3)C$: NNH_2·HCl solution for 30 s. Ammonium ferric sulfate solution ($NH_4Fe(SO_4)_2$·12H_2O, 1% w/w, 0.4 mL) was then added; the resulting mixture was shaken, and placed for 15 min in the dark. The final HCHO concentration was analyzed by the spectrophotometer at 630 nm.

3 Results and discussion

3.1 Characterization of Co-Mn precursor nanosheets

Free-standing $Co_xMn_{3-x}O_4$ nanosheets were grown on flexible carbon textile substrate by a facile anodic electrodeposition and a post-calcination treatment (details in Section 2.1). Figure 1(a) shows the SEM images of the Co-Mn precursor nanosheets. It can be seen that the Co-Mn precursor deposited on the carbon fiber has a thickness of ~20 nm and a width of ~200 nm. After annealing in air at 550 ˚C for 1 h, the Mn-Co precursor is successfully converted into $Co_xMn_{3-x}O_4$ corresponding to tetragonal $(Co,Mn)(Co,Mn)_2O_4$ (JCPDF #18-0408), which is confirmed by XRD analysis (Fig. 1(b)).

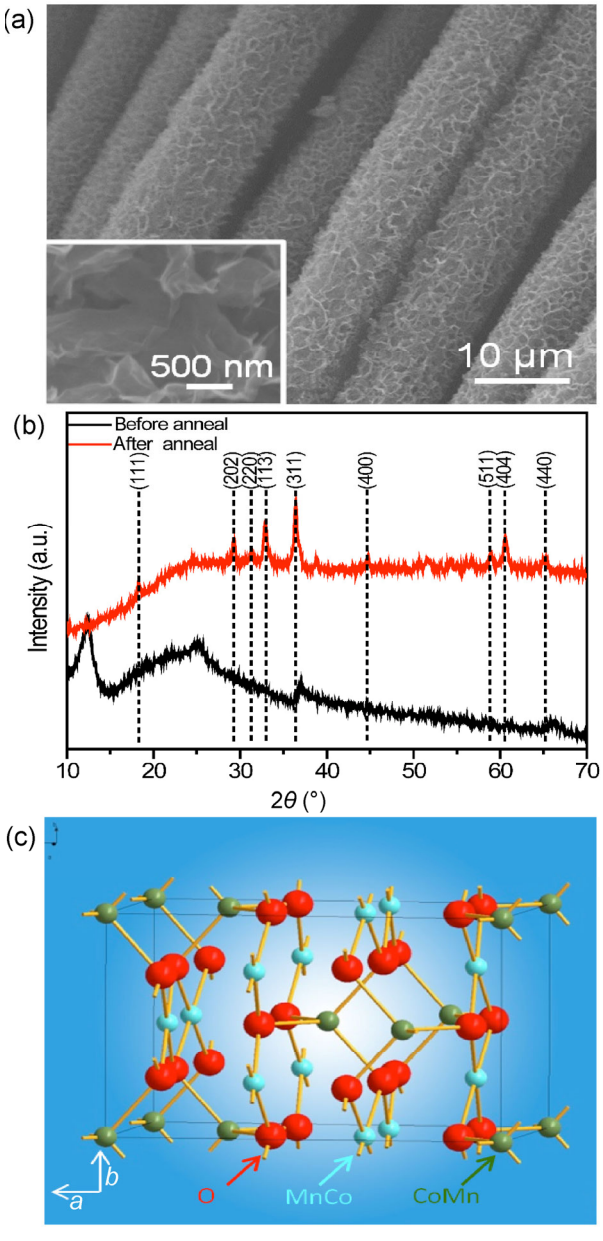

Figure 1 (a) SEM images of the Co-Mn precursor nanosheets on carbon textile. (b) XRD patterns of Co-Mn oxides nanowires before and after annealing. (c) Schematic illustration of the crystal structure of tetragonal $Co_xMn_{3-x}O_4$.

In this structure, cobalt and manganese occupy the tetragonal sites randomly but proportionally, as illustrated in Fig. 1(c). Moreover, the compositions of $Co_xMn_{3-x}O_4$ samples can be readily controlled by this present electrodeposition approach. For instance, $Co_xMn_{3-x}O_4$ products with different Mn/Co ratios such as $Co_{0.78}Mn_{2.22}O_4$, $Co_{0.70}Mn_{2.30}O_4$, $Co_{0.65}Mn_{2.35}O_4$, $Co_{0.58}Mn_{2.42}O_4$, and $Co_{0.43}Mn_{2.57}O_4$ are easily obtained by adjusting the ratio of Mn/Co in the precursor electrolyte (Fig. S1 in the Electronic Supplementary Material (ESM)).

3.2 Morphology of $Co_xMn_{3-x}O4$ nanosheets

Figures 2(a)–2(e) show SEM images of $Co_xMn_{3-x}O_4$ nanosheets. SEM studies show that all the samples are uniformly coated on the carbon textile substrates and have a thickness of ~20 nm and a width of ~200 nm. All the samples have a similar sheet-like morphology and the films are still very flexible. In order to study in detail the microstructure of $Co_{0.65}Mn_{2.35}O_4$ nanosheets (with optimized catalytic performance), TEM analysis was conducted. A typical TEM image of $Co_{0.65}Mn_{2.35}O_4$ nanosheets is shown in Fig. 2(f), which clearly shows the nanosheets. Selected-area electron diffraction (SAED) analysis shows that the $Co_{0.65}Mn_{2.35}O_4$ nanosheets have a poly-crystalline structure (the inset in Fig. 2(f)). To confirm the phase distribution, we collected high-resolution TEM (HRTEM) images of the nanosheets, as shown in Fig. 2(g). Well-resolved lattice fringes of 0.18, 0.20, and 0.24 nm corresponding to the (224), (400), and (311) interplanar spacing, respectively, of $(Co,Mn)(Co,Mn)_2O_4$ are clearly observed. Additionally, energy dispersive X-ray spectroscopy (EDS) elemental mapping data shows that O (red), Mn (green), and Co (yellow) elements are uniformly distributed in the nanosheets (Fig. 2(h)).

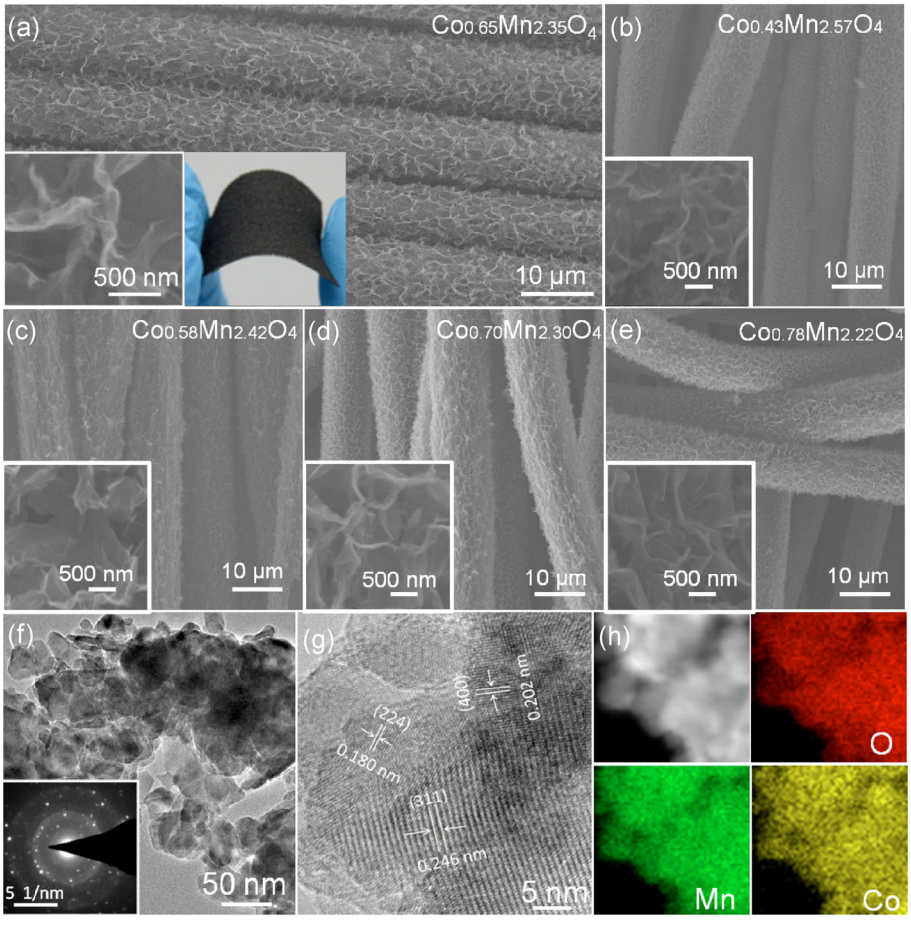

Figure 2 (a)–(e) SEM images of $Co_{0.65}Mn_{2.35}O_4$, $Co_{0.43}Mn_{2.57}O_4$, $Co_{0.58}Mn_{2.42}O_4$, $Co_{0.70}Mn_{2.30}O_4$, and $Co_{0.78}Mn_{2.22}O_4$ on a carbon textile. (f) TEM image and SAED pattern of $Co_{0.65}Mn_{2.35}O_4$ nanosheets. (g) HRTEM image of $Co_{0.65}Mn_{2.35}O_4$ nanosheets. (h) EDS elemental mapping of the same region, indicating spatial distribution of O (red), Mn (green) and Co (yellow), respectively.

All these results reveal the successful fabrication of $Co_xMn_{3-x}O_4$ nanosheets.

3.3 XRD analysis and XPS studies of the $Co_xMn_{3-x}O_4$ catalysts

In order to analyze the crystal quality of the $Co_xMn_{3-x}O_4$ nanosheets, further XRD analysis was carried out. Figure 3(a) shows the XRD patterns of all the $Co_xMn_{3-x}O_4$ nanosheets. It can be seen that all $Co_xMn_{3-x}O_4$ nanosheets have the same diffraction peaks. The diffraction features centered at about 18.2°, 29.3°, 31.3°, 32.9°, 44.8°, 59.1°, 60.6° and 65.2° correspond to the (111), (202), (220), (113), (400), (511), (404) and (440) planes of the tetragonal structure of the $(Co,Mn)(Co,Mn)_2O_4$ (JCPDF #18-0408). The narrow diffraction peaks and the intensities are weak, which indicates a low degree of crystallization of all synthesized $Co_xMn_{3-x}O_4$ nanosheets. Furthermore, the compositions of the nanosheets were analyzed by XPS, confirming that the nanosheets are oxides of Mn-Co. Figure S2 (in the ESM) displays the XPS spectra of all the $Co_xMn_{3-x}O_4$ nanosheets. Mn, Co, and O are the only elements observed in the $Co_xMn_{3-x}O_4$ nanosheet samples. The typical patterns of Co 2p are presented in Fig. 3(b). The curve of the Co 2p spectra at binding energies of 779.9 and 782.5 eV correspond to Co^{3+} and Co^{2+}, respectively [28]. It can be seen that the content of Co^{3+} in the different $Co_xMn_{3-x}O_4$ nanosheet sample surfaces increases in this order: $Co_{0.65}Mn_{2.35}O_4$ > $Co_{0.70}Mn_{2.30}O_4$ > $Co_{0.58}Mn_{2.42}O_4$ > $Co_{0.78}Mn_{2.22}O_4$ > $Co_{0.43}Mn_{2.57}O_4$. Abundant Co^{3+} ions possibly increase the anionic defect position, which is beneficial to catalytic oxidation. Figure 3(c) shows the XPS spectra of Mn 2p in the $Co_xMn_{3-x}O_4$ nanosheets. It is well known the binding energies around 643 and 641 eV can be attributed to the presence of Mn^{4+} and Mn^{3+} species, respectively [28]. It can be seen that the dominant manganese species in the $Co_{0.78}Mn_{2.22}O_4$ sample is Mn^{4+}, whereas that in the $Co_{0.43}Mn_{2.57}O_4$ sample is Mn^{3+} with only small amounts of Mn^{4+}. Interestingly, with an increasing amount of Mn in $Co_xMn_{3-x}O_4$ nanosheets, the Mn^{3+} content also increases. Our previous works consider

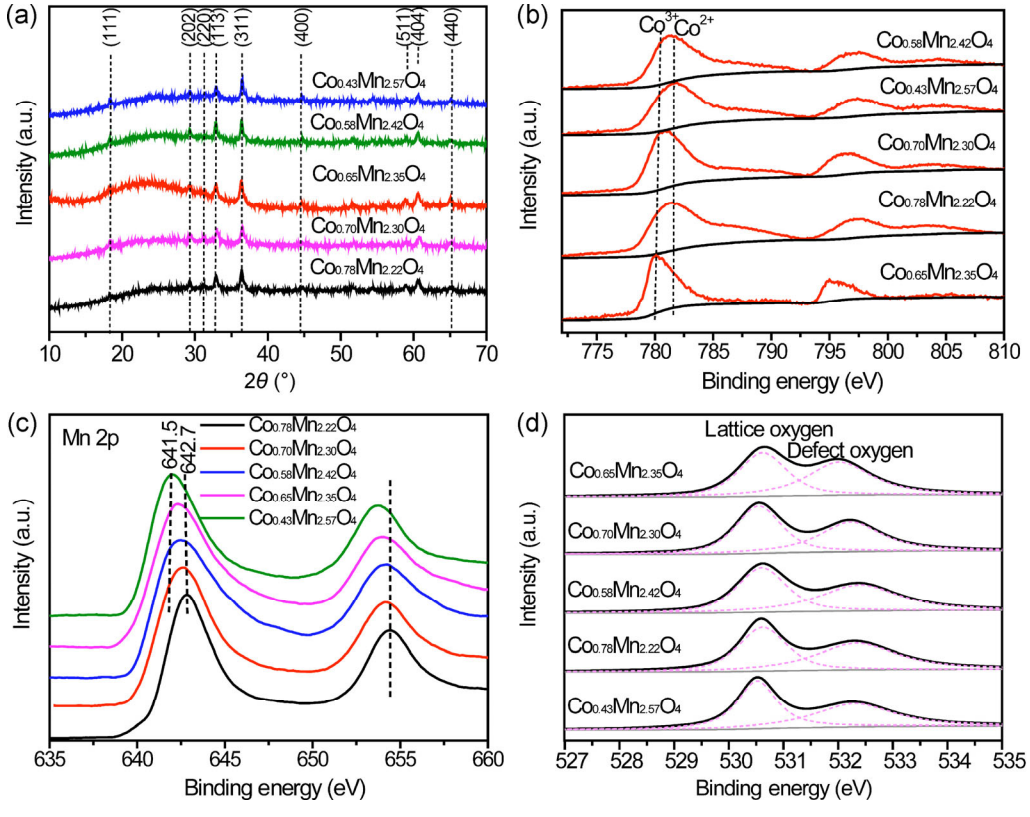

Figure 3 (a) XRD patterns, (b) Co 2p XPS spectra, (c) Mn 2p XPS spectra and (d) Core level O 1s XPS spectra of the $Co_xMn_{3-x}O_4$ catalysts.

that surface oxygen species play an important role in the activity of a catalyst [24, 29]. Figure 3(d) is the O 1s XPS diagram of the $Co_xMn_{3-x}O_4$ nanosheets. Obviously, there are two strong peaks at 530.5 and 532.5 eV. The peak at 530.5 eV is the characterization of lattice oxygen while the peak at 532.5 eV is attributed to the surface adsorbed oxygen. Table 1 shows a difference in the amount of surface adsorbed oxygen and lattice oxygen between the $Co_xMn_{3-x}O_4$ samples. Quantitative analysis further shows the surface adsorption oxygen population increases from 29.6% to 45.3% according to the order of the samples: $Co_{0.43}Mn_{2.57}O_4$ < $Co_{0.78}Mn_{2.22}O_4$ < $Co_{0.58}Mn_{2.42}O_4$ < $Co_{0.70}Mn_{2.30}O_4$ < $Co_{0.65}Mn_{2.35}O_4$. Meanwhile the lattice oxygen population decreases from 70.4% to 54.7%. It has been observed that upon changing the metal in the B sites of cobaltite, the surface oxygen adsorption also changes, because the cations placed in these sites play an important role in assisting the chemisorption of O_2 through their cationic d-orbitals [30]. This is beneficial for the formation of oxygen vacancies with more lattice defects, which can adsorb, activate oxygen gas, and provide the lattice sites for oxygen migration. The mobility of surface oxygen can be greatly improved with more defective oxygen on the surface. As an oxide catalyst for hydrocarbon oxidation, higher lattice oxygen mobility usually leads to higher catalytic activity [30]. A similar behavior has been reported in other oxides and perovskites for hydrocarbon oxidation [20, 31–33]. Therefore, $Co_{0.65}Mn_{2.35}O_4$ has the highest surface oxygen adsorption, which could account for its superior catalytic performance over the other catalysts.

3.4 Specific surface area measurements

The porous structure and texture of $Co_xMn_{3-x}O_4$ catalysts were investigated by N_2 sorption analysis. Figure 4 shows the nitrogen adsorption–desorption isotherms for $Co_xMn_{3-x}O_4$ catalysts. The result obtained from the N_2 adsorption shows that the entire samples exhibit similar isotherms and can be classified as type IV, possessing a distinct H3-type hysteresis loop at relative pressure ranges from 0.7–1.0 P/P_o, and revealing the typical mesoporous characteristics of the $Co_xMn_{3-x}O_4$ catalysts [29]. The pore structure parameters for all the $Co_xMn_{3-x}O_4$ catalysts are listed in Table 1, such as Brunauer–Emmett–Teller (BET) specific surface area, pore volume, and pore width. The $Co_xMn_{3-x}O_4$ catalysts exhibited similar BET values around 11.1–11.6 $m^2 \cdot g^{-1}$, indicating a minor effect of the surface area on the catalytic performance of the samples.

3.5 TPR and TPD measurements

The H_2-TPR patterns of the as-prepared $Co_xMn_{3-x}O_4$ catalysts are illustrated in Fig. 5(a). All the $Co_xMn_{3-x}O_4$ samples present a distinct H_2 consumption peak above 380 ℃. Importantly, a significant enhancement in the reducibility is observed for the $Co_{0.65}Mn_{2.35}O_4$ sample. There are reduction bands at ca. 208, 280 and 375 ℃. It is reasonable to deduce that the peak at ca. 208 ℃ is due to the reduction of surface oxygen species generated and the presence of more oxygen vacancies in $Co_{0.65}Mn_{2.35}O_4$. The peaks at ca. 280 and 375 ℃ are ascribed to the stepwise reduction of $Co_{0.65}Mn_{2.35}O_4$, involving the bulk oxygen species of cobalt and manganese oxides in mixed valences. The reduction peaks (208 and 280 ℃) make the main contribution to HCHO oxidation, compared with the other reduction peaks at the higher temperature of 375 ℃. Such low temperature desorption peaks

Table 1 Summary of the determination and quantitative analysis for surface oxygen and specific surface areas

Sample	Lattice oxygen	Surface adsorption oxygen	BET surface area ($m^2 \cdot g^{-1}$)	Pore volume ($cm^3 \cdot g^{-1}$)	Pore size (Å)
$Co_{0.65}Mn_{2.35}O_4$	54.7%	45.3%	11.6	0.09	248.6
$Co_{0.70}Mn_{2.30}O_4$	59.2%	40.8%	11.6	0.08	254.6
$Co_{0.58}Mn_{2.42}O_4$	62.8%	37.2%	11.06	0.07	245.4
$Co_{0.78}Mn_{2.22}O_4$	66.3%	32.7%	11.4	0.07	239.6
$Co_{0.43}Mn_{2.57}O_4$	70.4%	29.6%	11.5	0.08	254.2

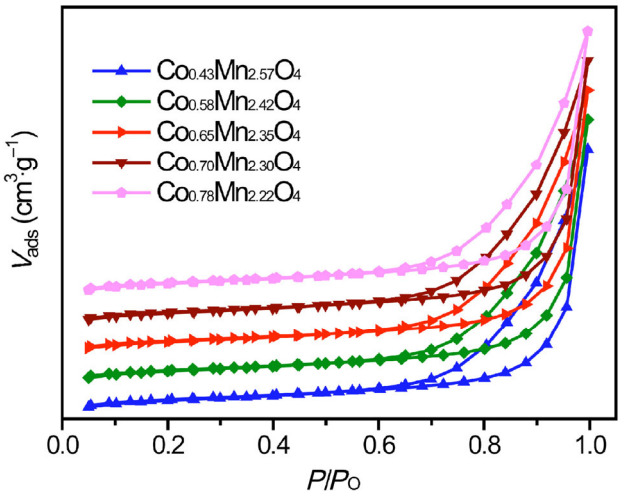

Figure 4 Nitrogen adsorption–desorption isotherm of the $Co_xMn_{3-x}O_4$ catalysts.

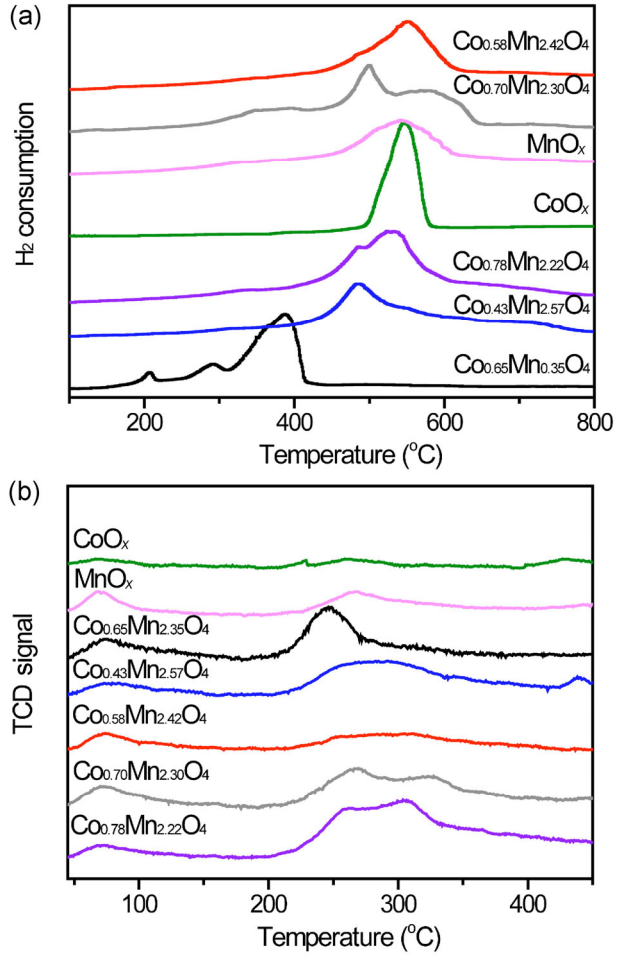

Figure 5 (a) H_2-TPR profiles and (b) O_2-TPD patterns of the $Co_xMn_{3-x}O_4$, CoO_x and MnO_x catalysts.

(around 200–350 ℃) have been shown to generate surface active oxygen species, leading to enhanced catalytic activity in oxidation reactions [15].

Figure 5(b) shows that the desorption peaks that are lower than 450 ℃ belong to the surface active oxygen, such as O_2^- and O^-. O_2^- and O^- are adsorbed molecular oxygen and surface adsorbed chemical oxygen, respectively, and belong to the surface active oxygen. These are easy to desorb from the metal oxide. All the catalysts have the desorption peak at 80 ℃, which belongs to the oxygen desorption. The presented peak at 245 ℃—which is lower than the other catalysts—as well as the higher peak intensity of the $Co_{0.65}Mn_{2.35}O_4$ catalyst over its counterparts indicates that the $Co_{0.65}Mn_{2.35}O_4$ surface has abundant surface active oxygen species (O_2^- and O^-). According to other reports, the desorption temperature and intensity of catalytic materials is connected to their catalytic oxidation activity [14, 19]. Lower initial oxygen desorption temperatures and larger intensities of desorption peaks correspond to better catalytic ability.

It can be seen that the TPR of CoO_x nanosheet sample show one peak at 530 ℃, which is the same as reported elsewhere [23]. The H_2-TPR profile of MnO_x sample displays one overlapped reduction peak at 456.9–616.0 ℃. The broad peak represents the sequential reduction of MnO_2 to Mn_3O_4 and Mn_3O_4 to MnO. According to Fig. 5(b), the TPD pattern of MnO_x sample displays two desorption peaks; one at 80 ℃, which indicates the presence of O_2^- species. This is compared to that of the CoO_x nanosheet sample, which has almost no active oxygen peaks before 450 ℃. Comparing the TPR and TPD patterns of MnO_x and CoO_x nanosheets with those of $Co_xMn_{3-x}O_4$ nanosheet sample, we can conclude that surface defective oxygen species are the reason for the high activity. The $Co_{0.65}Mn_{2.35}O_4$ has the best catalytic activity due to the abundance of active surface oxygen species that can easily participate in the catalytic oxidation reaction.

The formaldehyde oxidation over $Co_xMn_{3-x}O_4$ nanosheets is schematically shown in Scheme 1. The synergistic effect between the manganese and surface defective oxygen in the $Co_xMn_{3-x}O_4$ nanosheets can be essentially considered as a process of oxygen activation and oxygen transfer through the redox cycles of Mn^{4+}/Mn^{3+} and Co^{3+}/Co^{2+}. Therefore, based

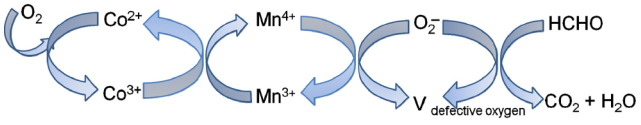

Scheme 1 Schematic illustration of HCHO oxidation over Co_xMn_{3-x} nanosheets.

on the above analyses, the abundant active surface oxygen species and excellent redox ability are believed to be the major reasons for the superior catalytic oxidation of HCHO.

3.6 Catalytic activity of $Co_xMn_{3-x}O_4$ nanosheets

HCHO oxidation is used as a probe reaction to understand the catalytic activities of the $Co_xMn_{3-x}O_4$ nanosheet catalysts. Pristine MnO_x nanosheets and CoO_x nanosheets are also studied for comparison (Figs. S3 and S4 in the ESM). Figure 6(a) shows the conversion efficiency with increasing reaction temperature over the different catalysts. All the $Co_xMn_{3-x}O_4$ nanosheets exhibited higher catalytic activities than the pristine MnO_x and CoO_x nanosheets. Particularly, the $Co_{0.65}Mn_{2.35}O_4$ nanosheets achieved a remarkably low "complete-conversion" temperature (100% of HCHO conversion is achieved) of 100 ˚C, which is substantially lower than that of $Co_{0.70}Mn_{2.30}O_4$ (110 ˚C), $Co_{0.58}Mn_{2.42}O_4$ (130 ˚C), $Co_{0.78}Mn_{2.22}O_4$ (140 ˚C), $Co_{0.43}Mn_{2.57}O_4$ (140 ˚C), MnO_x (170 ˚C), CoO_x (180 ˚C). Additionally, the complete-conversion temperature of the $Co_{0.65}Mn_{2.35}O_4$ is also considerably lower than the values recently reported for other Mn-based catalysts and some metal-oxide catalysts, such as 2.5% Au/CeO_2 (T_{100} = 75 ˚C, 50,000 mL·h^{-1}·g^{-1}) [31], MnO_x–CeO_2 (T_{100} = 150 ˚C, 60,000 mL·h^{-1}·g^{-1}) [34], 3D-Co_3O_4 (T_{100} = 130 ˚C, 30,000 mL·h^{-1}·g^{-1}) [19], mesoporous MnO_x (T_{100} = 160 ˚C, 30,000 mL·h^{-1}·g^{-1}) [35], MnO_x–SnO_2 (T_{100} = 180 ˚C, 30,000 mL·h^{-1}·g^{-1}) [36], MnO_2/cellulose (T_{100} = 150 ˚C, 50,000 mL·h^{-1}·g^{-1}) [37], hollow K_xMnO_2 nanospheres (T_{100} = 140 ˚C, 50,000 mL·h^{-1}·g^{-1}) [10], 0.34% Au/CeO_2 (T_{100} = 140 ˚C, 34,000 mL·h^{-1}·g^{-1}) [38], and slightly higher than the 3D-$Mn_{0.75}Co_{2.25}O_4$ (T_{100} = 75 ˚C, 120,000 mL·h^{-1}·g^{-1}) [23]. Furthermore, the light-off temperature (i.e., the temperature at which 10% conversion is achieved) of the $Co_{0.65}Mn_{2.35}O_4$ (20 ˚C) is also much lower than that of pristine MnO_x (60 ˚C), CoO_x (100 ˚C), and other $Co_xMn_{3-x}O_4$ samples (40–60 ˚C). These results suggest that the different content of Co could be an influence on HCHO oxidation and results in $Co_{0.65}Mn_{2.35}O_4$ being an effective catalyst for HCHO oxidation.

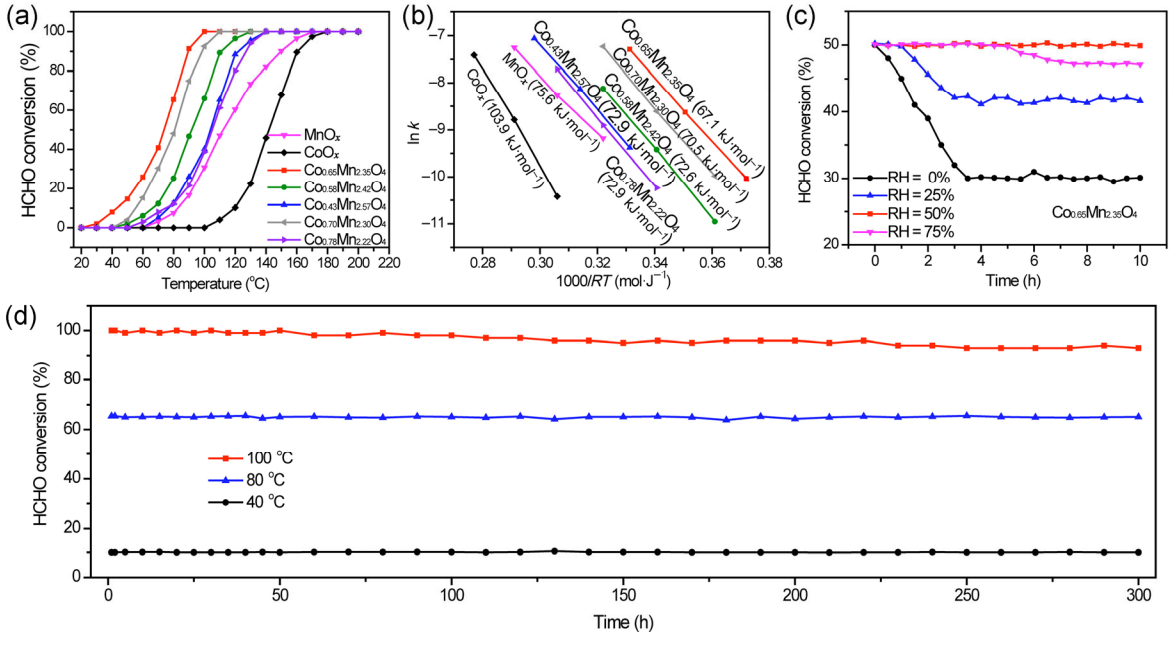

Figure 6 (a) Catalytic performance of HCHO over all catalysts with increasing reaction temperature under the following conditions: HCHO concentration = 50 ppm, 25 vol.% O_2, N_2 as balance gas, RH = 50%, The hourly space velocity (GSHV) = 120,000 mL·h^{-1}·g^{-1}. (b) Arrhenius plots for total oxidation of HCHO on the all catalysts. (c) Effect of relative humidity on removal efficiency of HCHO over $Co_{0.65}Mn_{2.35}O_4$ nanosheet at 75 ˚C. (d) Catalytic performance of HCHO over $Co_{0.65}Mn_{2.35}O_4$ at 100, 80 and 40 ˚C as long as 300 h.

To gain insight into the effect of varying Co content on HCHO oxidation over $Co_xMn_{3-x}O_4$ catalysts, we carried out kinetics tests over the $Co_xMn_{3-x}O_4$ catalysts. Figure 6(b) shows Arrhenius plots for the catalysts of HCHO oxidation at lower than 100% conversion. The apparent activation energy (E_a) of the HCHO oxidation reaction is 103.9 kJ·mol^{-1} for the CoO_x sample, which is much higher than the $Co_xMn_{3-x}O_4$ catalysts (67.1–75.6 kJ·mol^{-1}). The lowest activation energy was obtained for $Co_{0.65}Mn_{2.35}O_4$ confirming that the HCHO oxidation reaction is much easier over the $Co_{0.65}Mn_{2.35}O_4$ catalyst surface than its counterparts. Furthermore, the complete conversion (100%) is obtained at or above 100 ˚C, which is influenced by the varying content of Co. Notably, with an increase of Co to 21%, HCHO conversion is obviously improved, which is shown in Fig. S5 (in the ESM). The complete conversion is obtained at 100 ˚C, while it is decreased to 69.9% with the further increase in Co content. These results also indicate that the Co content has a positive effect on HCHO oxidation over $Co_xMn_{3-x}O_4$ catalyst. Therefore, based on the above results, we can validate that the $Co_{0.65}Mn_{2.35}O_4$ nanosheets possess significantly high catalytic activity for HCHO oxidation at low temperature.

3.6.1 *Catalysis under humid conditions*

Humidity is a key factor in the catalytic oxidation of HCHO. In order to study the effect of humidity on this reaction, the influence of humidity was investigated on the $Co_{0.65}Mn_{2.35}O_4$ nanosheet at 75 ˚C, which is shown in Fig. 6(c). Exposed to dry air, there is only 29% HCHO conversion after 3.5 h of reaction time. However, when the relative humidity (RH) increased to 50%, the content of H_2O is high enough to sustain the catalytic process and no significant deactivation was observed. The activity of HCHO decreased to 44% after 10 h of reaction, when the relative humidity increased to 75% due to the competitive adsorption of water and HCHO on the catalyst surface. Thus, humidity plays an important role on the catalytic oxidation of HCHO.

From a practical point of view, stability issues should be taken into account when considering catalysts for catalytic reactions. Figure 6(d) displays the catalytic oxidation performance of HCHO over $Co_{0.65}Mn_{2.35}O_4$ nanosheets on stream at 100, 80, and 40 ˚C, respectively. At the end of 300 h, the $Co_{0.65}Mn_{2.35}O_4$ nanosheets achieved an exemplary long-term stability, with little decline in its HCHO conversion efficiency. This strongly proves the catalytic stability of the $Co_{0.65}Mn_{2.35}O_4$ nanosheets. To further demonstrate the durability of the $Co_{0.65}Mn_{2.35}O_4$ nanosheets, SEM and XRD tests were carried out after long cycling at 100 ˚C. It is notable that the nanosheet structure of the $Co_{0.65}Mn_{2.35}O_4$ can still be clearly identified after the long cycling process (Fig. 7(a)); likewise, the XRD spectra show that the phase and chemical compositions of the $Co_{0.65}Mn_{2.35}O_4$ are still maintained without glaring changes (Fig. 7(b)). Thus, we conclude that the excellent stability of the $Co_{0.65}Mn_{2.35}O_4$ nanosheet can be attributed to its excellent structural stability, phase stability, and the mechanical support from the flexible carbon fiber.

3.7 Mechanism of the catalyzed HCHO oxidation reaction

To investigate the adsorption behaviors of the reactant molecules on the surface of the $Co_{0.65}Mn_{2.35}O_4$ catalysts,

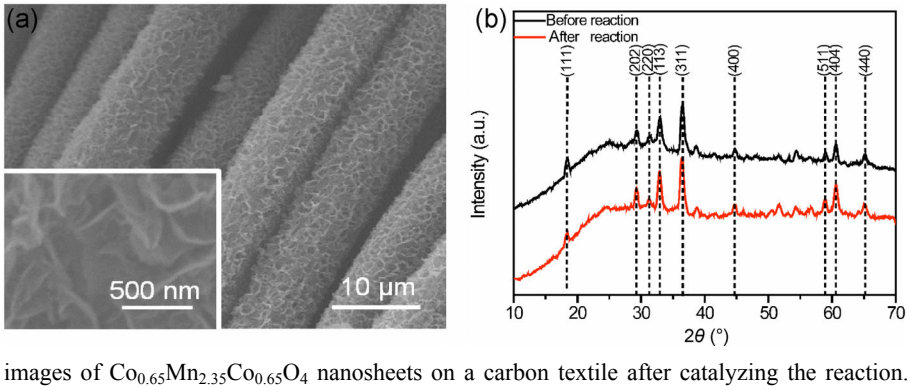

Figure 7 (a) SEM images of $Co_{0.65}Mn_{2.35}Co_{0.65}O_4$ nanosheets on a carbon textile after catalyzing the reaction. (b) XRD pattern of $Co_{0.65}Mn_{2.35}O_4$ nanosheets before and after the reaction.

the *in situ* DRIFTS experiments were performed. Figure 8(a) shows the DRIFT spectra recorded under a stream of N_2 co-eluted with 21% O_2 and a RH of 50% at elevated temperatures after the catalyst was first exposed to a flow of 50 ppm HCHO in the same carrier gas composition for 60 min. Upon exposure to a humid air stream (50 ppm HCHO/21% O_2/N_2 balance), peaks ascribed to formate species (1,573 and 1,360 cm^{-1}), hydrocarbonates (1,603 and 1,420 cm^{-1}), and water (1,640 cm^{-1}) appeared. These results are indicative of the partial oxidation of HCHO to form formate species, which could further combine with surface oxygen to form hydrocarbonate [3]. The bands attributed to hydrocarbonate and adsorbed H_2O rapidly decreased in intensity with increasing temperature. Upon heating to 85 °C, the characteristic peaks due to hydrocarbonate disappeared, while only weakly adsorbed H_2O could be observed. This temperature coincided with that at which 100% conversion of HCHO is obtained. Therefore, it is suggested that the HCHO oxidation reaction on samples follows the formate ($HCOO^-$) decomposition route ($HCHO \rightarrow HCOO^- \rightarrow CO \rightarrow CO_2$). In order to further confirm the presence of CO_2 in the effluent gases, the CO_2 in the gas phase is determined by an on-line mass spectrometer analyzer. From Fig. 8(b) we can observe that the fragmentation intensities of CO_2 (m/z = 44) reached a steady level.

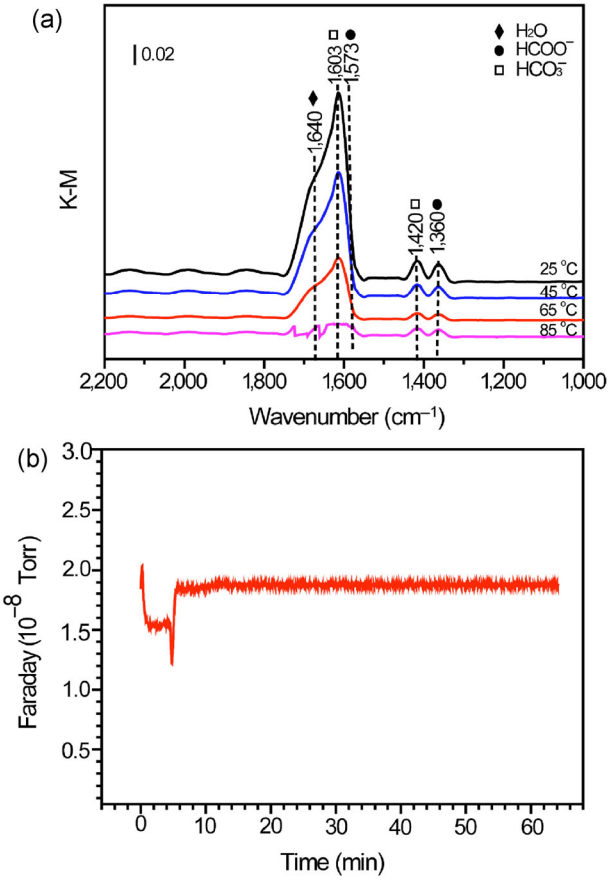

Figure 8 (a) DRIFTs spectra collected over $Co_{0.65}Mn_{2.35}O_4$ upon temperature rise. (b) Mass spectrometer spectra recorded from $Co_{0.65}Mn_{2.35}O_4$ at the relative molecular mass of 44 for periods up to 60 min.

4 Conclusions

In summary, flexible 3D $Co_xMn_{3-x}O_4$ nanosheets were shown to be stable, low-cost, and high-performance catalysts for low-temperature thermal catalytic oxidation of HCHO. The mesoporous $Co_xMn_{3-x}O_4$ nanosheets were grown on carbon textile substrates with robust adhesion property by electrodeposition and post-annealing. $Co_{0.65}Mn_{2.35}O_4$ exhibited superior catalytic activity that could convert 100% of HCHO at a low temperature of 100 °C. The catalytic activity was considerably higher than that of most non-precious metal-based catalysts at such temperatures. Furthermore, the $Co_{0.65}Mn_{2.35}O_4$ nanosheets exhibited a remarkable long-term durability, which is significant for practical uses.

Acknowledgements

This work was preliminarily supported by the National Natural Science Foundation of China (Nos. 21425627 and 21276104) and Natural Science Foundation of Guangdong Province (Nos. 21425627).

Electronic Supplementary Material: Supplementary material (atomic ratio of catalysts, XPS survey spectra, SEM, and XRD of the catalysts) is available in the online version of this article at http://dx.doi.org/10.1007/s12274-016-1257-9.

References

[1] Bai, B. Y.; Li, J. H. Positive effects of K^+ ions on three-dimensional mesoporous Ag/Co_3O_4 catalyst for HCHO oxidation. *ACS Catal.* **2014**, *4*, 2753–2762.

[2] Fan, W. J.; Li, H. B.; Zhao, F. Y.; Xiao, X. J.; Huang, Y. C.; Ji, H. B; Tong, Y. X. Boosting the photocatalytic performance of (001) BiOI: Enhancing donor density and separation efficiency of photogenerated electrons and holes. *Chem. Commun.* **2016**, *52*, 5316–5319.

[3] Huang, H. B.; Xu, Y.; Feng, Q. Y.; Leung, D. Y. C. Low temperature catalytic oxidation of volatile organic compounds: A review. *Catal. Sci. Technol.* **2015**, *5*, 2649–2669.

[4] Qi, J.; Chen, J.; Li, G. D.; Li, S. X.; Gao, Y.; Tang, Z. Y. Facile synthesis of core-shell Au@CeO_2 nanocomposites with remarkably enhanced catalytic activity for CO oxidation. *Energy Environ. Sci.* **2012**, *5*, 8937–8941.

[5] Xu, Q. L.; Lei, W. Y.; Li, X. Y.; Qi, X. Y.; Yu, J. G.; Liu, G.; Wang, J. L.; Zhang, P. Y. Efficient removal of formaldehyde by nanosized gold on well-defined CeO_2 nanorods at room temperature. *Environ. Sci. Technol.* **2014**, *48*, 9702–9708.

[6] Zhang, C. B.; Liu, F. D.; Zhai, Y. P.; Ariga, H.; Yi, N.; Liu, Y. C.; Asakura, K.; Flytzani-Stephanopoulos, M.; He, H. Alkali-metal-promoted Pt/TiO_2 opens a more efficient pathway to formaldehyde oxidation at ambient temperatures. *Angew. Chem., Int. Ed.* **2012**, *51*, 9628–9632.

[7] Huang, Y. C.; Li, H. B.; Balogun, M. S.; Yang, H.; Tong, Y. X.; Lu, X. H.; Ji, H. B. Three-dimensional TiO_2/CeO_2 nanowire composite for efficient formaldehyde oxidation at low temperature. *RSC Adv.* **2015**, *5*, 7729–7733.

[8] Jin, M. S.; Zhang, H.; Xie, Z. X.; Xia, Y. N. Palladium nanocrystals enclosed by {100} and {111} facets in controlled proportions and their catalytic activities for formic acid oxidation. *Energy Environ. Sci.* **2012**, *5*, 6352–6357.

[9] Xu, Z. H.; Yu, J. G.; Low, J. X.; Jaroniec, M. Microemulsion-assisted synthesis of mesoporous aluminum oxyhydroxide nanoflakes for efficient removal of gaseous formaldehyde. *ACS Appl. Mater. Interfaces* **2014**, *6*, 2111–2117.

[10] Chen, H. M.; He, J. H.; Zhang, C. B.; He, H. Self-assembly of novel mesoporous manganese oxide nanostructures and their application in oxidative decomposition of formaldehyde. *J. Phys. Chem. C* **2007**, *111*, 18033–18038.

[11] Zhang, J. H.; Li, Y. B.; Wang, L.; Zhang, C. B.; He, H. Catalytic oxidation of formaldehyde over manganese oxides with different crystal structures. *Catal. Sci. Technol.* **2015**, *5*, 2305–2313.

[12] Yao, X. J.; Xiong, Y.; Zou, W. X.; Zhang, L.; Wu, S. G.; Dong, X.; Gao, F.; Deng, Y.; Tang, C. J.; Chen, Z. et al. Correlation between the physicochemical properties and catalytic performances of $Ce_xSn_{1-x}O_2$ mixed oxides for NO reduction by CO. *Appl. Catal. B: Environ.* **2014**, *144*, 152–165.

[13] Hu, L. H.; Sun, K. Q.; Peng, Q.; Xu, B. Q.; Li, Y. D. Surface active sites on Co_3O_4 nanobelt and nanocube model catalysts for CO oxidation. *Nano Res.* **2010**, *3*, 363–368.

[14] Huang, H. B.; Leung, D. Y. C. Complete oxidation of formaldehyde at room temperature using TiO_2 supported metallic Pd nanoparticles. *ACS Catal.* **2011**, *1*, 348–354.

[15] Chen, B. B.; Shi, C.; Crocker, M.; Wang, Y.; Zhu, A. M. Catalytic removal of formaldehyde at room temperature over supported gold catalysts. *Appl. Catal. B: Environ.* **2013**, *132-133*, 245–255.

[16] Zhang, C. X.; Li, S. R.; Wang, T.; Wu, G. W.; Ma, X. B.; Gong, J. L. Pt-based core–shell nanocatalysts with enhanced activity and stability for CO oxidation. *Chem. Commun.* **2013**, *49*, 10647–10649.

[17] Ma, Z.; Dai, S. Development of novel supported gold catalysts: A materials perspective. *Nano Res.* **2011**, *4*, 3–32.

[18] Liu, J. F.; Chen, W.; Liu, X. W.; Zhou, K. B.; Li, Y. D. Au/$LaVO_4$ nanocomposite: Preparation, characterization, and catalytic activity for CO oxidation. *Nano Res.* **2008**, *1*, 46–55.

[19] Bai, B. Y.; Arandiyan, H.; Li, J. H. Comparison of the performance for oxidation of formaldehyde on nano-Co_3O_4, 2D-Co_3O_4, and 3D-Co_3O_4 catalysts. *Appl. Catal. B: Environ.* **2013**, *142–143*, 677–683.

[20] Liotta, L. F.; Ousmane, M.; Di Carlo, G.; Pantaleo, G.; Deganello, G.; Marcì, G.; Retailleau, L.; Giroir-Fendler, A. Total oxidation of propene at low temperature over Co_3O_4–CeO_2 mixed oxides: Role of surface oxygen vacancies and bulk oxygen mobility in the catalytic activity. *Appl. Catal. A: Gen.* **2008**, *347*, 81–88.

[21] Zhen, J. M.; Wang, X.; Liu, D. P.; Wang, Z.; Li, J. Q.; Wang, F.; Wang, Y. H.; Zhang, H. J. Mass production of Co_3O_4@CeO_2 core@shell nanowires for catalytic CO oxidation. *Nano Res.* **2015**, *8*, 1944–1955.

[22] Shi, C.; Wang, Y.; Zhu, A. M.; Chen, B. B.; Au, C. $Mn_xCo_{3-x}O_4$ solid solution as high-efficient catalysts for low-temperature oxidation of formaldehyde. *Catal. Commun.* **2012**, *28*, 18–22.

[23] Wang, Y.; Zhu, X. B.; Crocker, M.; Chen, B. B.; Shi, C. A comparative study of the catalytic oxidation of HCHO and CO over $Mn_{0.75}Co_{2.25}O_4$ catalyst: The effect of moisture. *Appl. Catal. B: Environ.* **2014**, *160–161*, 542–551.

[24] Huang, Y. C.; Fan, W. J.; Long, B.; Li, H. B.; Qiu, W. T.; Zhao, F. Y.; Tong, Y. X.; Ji, H. B. Alkali-modified non-precious metal 3D-$NiCo_2O_4$ nanosheets for efficient formaldehyde oxidation at low temperature. *J. Mater. Chem. A* **2016**, *4*, 3648–3654.

[25] Maliyekkal, S. M.; Lisha, K. P.; Pradeep, T. A novel cellulose–manganese oxide hybrid material by *in situ* soft chemical synthesis and its application for the removal of Pb(II) from water. *J. Hazard. Mater.* **2010**, *181*, 986–995.

[26] Subramanian, V.; Zhu, H. W.; Wei, B. Q. Alcohol-assisted room temperature synthesis of different nanostructured

manganese oxides and their pseudocapacitance properties in neutral electrolyte. *Chem. Phys. Lett*. **2008**, *453*, 242–249.

[27] Balogun, M.-S.; Qiu, W. T.; Lyu, F. Y.; Luo, Y.; Meng, H.; Li, J. T.; Mai, W. J.; Mai, L. Q.; Tong, Y. X. All-flexible lithium ion battery based on thermally-etched porous carbon cloth anode and cathode. *Nano Energy* **2016**, *26*, 446–455.

[28] Quiroz, J.; Giraudon, J.-M.; Gervasini, A.; Dujardin, C.; Lancelot, C.; Trentesaux, M.; Lamonier, J. F. Total oxidation of formaldehyde over MnO_x-CeO_2 catalysts: The effect of acid treatment. *ACS Catal*. **2015**, *5*, 2260–2269.

[29] Huang, Y. C.; Long, B.; Tang, M. N.; Rui, Z. B.; Balogun, M. S.; Tong, Y. X.; Ji, H. B. Bifunctional catalytic material: An ultrastable and high-performance surface defect CeO_2 nanosheets for formaldehyde thermal oxidation and photocatalytic oxidation. *Appl. Catal. B: Environ*. **2016**, *181*, 779–787.

[30] Ren, Z.; Botu, V.; Wang, S. B.; Meng, Y. T.; Song, W. Q.; Guo, Y. B.; Ramprasad, R.; Suib, S. L.; Gao, P. X. Monolithically integrated spinel $M_xCo_{3-x}O_4$ (M = Co, Ni, Zn) nanoarray catalysts: Scalable synthesis and cation manipulation for tunable low-temperature CH_4 and CO oxidation. *Angew. Chem., Int. Ed*. **2014**, *53*, 7223–7227.

[31] Li, H. F.; Zhang, N.; Chen, P.; Luo, M. F.; Lu, J. Q. High surface area Au/CeO_2 catalysts for low temperature formaldehyde oxidation. *Appl. Catal. B: Environ*. **2011**, *110*, 279– 285.

[32] McCarty, J. G.; Wise, H. Perovskite catalysts for methane combustion. *Catal. Today* **1990**, *8*, 231–248.

[33] Li, J. H.; Fu, H. J.; Fu, L. X.; Hao, J. M. Complete combustion of methane over indium tin oxides catalysts. *Environ. Sci. Technol*. **2006**, *40*, 6455–6459.

[34] Tang, X. F.; Li, Y. G.; Huang, X. M.; Xu, Y. D.; Zhu, H. Q.; Wang, J. G.; Shen, W. J. MnO_x–CeO_2 mixed oxide catalysts for complete oxidation of formaldehyde: Effect of preparation method and calcination temperature. *Appl. Catal. B: Environ*. **2006**, *62*, 265–273.

[35] Torres, J. Q.; Giraudon, J. M.; Lamonier, J. F. Formaldehyde total oxidation over mesoporous MnO_x catalysts. *Catal. Today* **2011**, *176*, 277–280.

[36] Wen, Y. R.; Tang, X.; Li, J. H.; Hao, J. M.; Wei, L. S.; Tang, X. F. Impact of synthesis method on catalytic performance of MnO_x–SnO_2 for controlling formaldehyde emission. *Catal. Commun*. **2009**, *10*, 1157–1160.

[37] Zhou, L.; He, J. H.; Zhang, J.; He, Z. C.; Hu, Y. C.; Zhang, C. B.; He, H. Facile *in-situ* synthesis of manganese dioxide nanosheets on cellulose fibers and their application in oxidative decomposition of formaldehyde. *J. Phys. Chem. C* **2011**, *115*, 16873–16878.

[38] Shen, Y. N.; Yang, X. Z.; Wang, Y. Z.; Zhang, Y. B.; Zhu, H. Y.; Gao, L.; Jia, M. L. The states of gold species in CeO_2 supported gold catalyst for formaldehyde oxidation. *Appl. Catal. B: Environ*. **2008**, *79*, 142–148.